ADVANCING EARTH AND SPACE SCIENCE

JGR Space Physics

RESEARCH ARTICLE
10.1029/2020JA029035

Key Points:

- High-speed jets are simulated with a three-dimensional hybrid code, HYPERS under quasi-radial interplanetary magnetic field conditions
- Properties of simulation jets, generated by the turbulent dynamics of magnetosheath plasma, are generally consistent with the observations
- Significant impacts of large magnetosheath jets on the cusp and the magnetopause are demonstrated

Correspondence to:
Y. A. Omelchenko,
omelche@gmail.com

Citation:
Omelchenko, Y. A., Chen, L.-J., & Ng, J. (2021). 3D space-time adaptive hybrid simulations of magnetosheath high-speed jets. *Journal of Geophysical Research: Space Physics*, *126*, e2020JA029035. https://doi.org/10.1029/2020JA029035

Received 14 DEC 2020
Accepted 15 JUN 2021

3D Space-Time Adaptive Hybrid Simulations of Magnetosheath High-Speed Jets

Y. A. Omelchenko[1,2], L.-J. Chen[3], and J. Ng[3,4]

[1]Trinum Research, Inc., San Diego, CA, USA, [2]Space Science Institute, Boulder, CO, USA, [3]NASA Goddard Space Flight Center, Greenbelt, MD, USA, [4]University of Maryland, College Park, MD, USA

Abstract We study the generation and evolution of spatially localized dynamic plasma pressure enhancements in the magnetosheath (high-speed jets) by carrying out three-dimensional hybrid simulations of the Earth's dayside magnetosphere with a novel, space-time adaptive code, HYPERS. High-speed jets are shown to occur downstream of quasi-parallel bow shocks under southward and northward quasi-radial interplanetary magnetic field conditions. The physical properties and three-dimensional morphology of simulation jets are found to be consistent with general statistical knowledge acquired from the satellite observations. We discuss a "magnetokinetic" mechanism for jet origin whereby the compression of solar wind plasma and its penetration into the magnetosheath is tied to the turbulence-driven magnetic field perturbations. We compare three-dimensional jets to dynamic pressure structures observed in two-dimensional hybrid simulations and demonstrate the impact of large jets on the magnetopause and the cusp.

Plain Language Summary We present results from two global three-dimensional simulations of the Earth's dayside magnetosphere performed with a novel hybrid code, HYPERS that adaptively selects asynchronous computational updates for electromagnetic fields and kinetic ions on a stretched computational mesh. These simulations are set up with a southward and northward quasi-radial interplanetary magnetic field to provide conditions for the reflecting ions to drive strong turbulence in the magnetosheath (the region of space between the magnetopause and the bow shock). We show that this turbulence creates entangled magnetic field lines. Sporadically moving in the magnetosheath, these field lines "funnel" the solar wind plasma deeper into the magnetosheath, thereby creating compact dynamic pressure enhancements, known as high-speed jets. We show that the properties of simulation jets are generally consistent with the observations. We also compare these jets to dynamic pressure structures generated in two-dimensional hybrid simulations and demonstrate the significant impact of large jets on the magnetopause and the cusp regions of the magnetosphere.

1. Introduction

Many transient physical processes operate simultaneously and couple nonlinearly in the near-Earth environment across turbulent spatio-temporal scales, producing strong impacts on the cusp, magnetopause and ionosphere that are difficult to fully understand and predict without kinetic simulations. In particular, under quasi-radial interplanetary magnetic field (IMF) conditions the turbulent magnetosheath flow generates large-amplitude, spatially localized dynamic pressure enhancements, known as magnetosheath jets or high-speed jets (Plaschke et al., 2018). These structures, commonly observed by satellites downstream of quasi-parallel bow shocks, carry significant amounts of momentum, energy and magnetic flux. Therefore, their generation mechanism, characteristic lifetimes, physical and geometric properties, and possible impact on the magnetosphere present strong interest to the space physics community.

Based on observations in the past two decades, a great amount of statistical knowledge, as well as possible theoretical explanations relating the occurrence of jets to solar wind and foreshock conditions, have been accumulated (Plaschke et al., 2018, 2020). In particular, a theory by Hietala et al. (2012, 2009) suggests that plasma ripples, which inherently develop in the bow shock under quasi-radial IMF and high Mach solar wind conditions, may be responsible for producing local high-speed flows in the magnetosheath by deflecting the incoming solar wind plasma flow in the anti-sunward direction due to the local curvature of a shock front so that the speed of the deflected flow remains close to the upstream solar wind value.

High-speed jets have also been compared to magnetotail bursty bulk flows. However, as noted by Plaschke et al. (2018), the closed topology of magnetic field lines in the plasma sheet is drastically different from that of the magnetosheath. Other theoretical explanations for jet generation, as reviewed by Plaschke et al. (2018), include interactions of solar wind discontinuities with the bow shock and magnetic reconnection inside the magnetosheath. Still, since these jets occur predominantly downstream of quasi-parallel shocks during periods of steady quasi-radial IMF, the search for their origin should naturally focus on physical processes that produce dynamic bow shock structures under these particular solar wind conditions.

As of today, global physical processes in the Earth's magnetosphere are predominantly modeled with magnetohydrodynamics (MHD) codes. The success of MHD comes at the expense of its reduced physics compared to the kinetic models which compute velocity distributions of plasma species and advance electromagnetic fields and particles on finer spatial meshes and faster time scales. It is well known, however, that under quasi-radial IMF conditions many observed physical phenomena cannot be satisfactorily reproduced by MHD models. Foreshock turbulence, resonant and stochastic ion acceleration by shocks, direct solar-wind ion injections into the cusp, ionospheric ion outflows energized to ring current energies, cascading of large-scale field-aligned currents into kinetic scales are just a few examples where ion kinetic effects become essential for interpreting spacecraft data in the near-Earth space environment.

While three-dimensional (3D) full-electromagnetic Particle-in-Cell (PIC) simulations of the Earth's magnetosphere are still computationally prohibitive, quasi-neutral radiation-free hybrid PIC codes, which treat ion species kinetically and electrons as a massless fluid (e.g., see a review by Winske et al., 2003), have demonstrated great success in predicting detailed plasma behavior. This has become possible because the hybrid models self-consistently account for a wide range of spatio-temporal scales that drive plasma instabilities and turbulence, as well as influence ion velocity distributions, as confirmed by numerous space observations and laboratory experiments.

In order to accurately represent mesoscale effects, global hybrid simulations need to resolve the ion inertial length and fast whistler time scales ~0.1 s in strong magnetic fields and low plasma density regions near the Earth, which is computationally prohibitive for a realistic dipole strength in 3D but feasible for a scaled-down magnetosphere. Given the solar wind proton inertial length, $d_i \sim 100$ km, and the Earth radius, $R_E \sim 60d_i$, the actual magnetopause stand-off distance, $R_M \sim (6\text{–}10)\ R_E \simeq (400\text{–}700)d_i$ in 3D hybrid simulations typically needs to be scaled down to $\sim 100d_i$, a size large enough to reproduce the important ion kinetic features of the magnetosphere (Omidi et al., 2004). Alternatively, d_i may be scaled up to produce faster simulation Alfvén speeds (Lin, 2003). For comparisons with observations, however, the stand-off distance in simulations is often specified in terms of the Earth radius, R_E. In what follows we assume $R_M = 10R_E$ for that purpose.

An important requirement for a robust magnetospheric hybrid code is its ability to accurately and efficiently compute dynamic plasma patterns that typically emerge in global simulations under strong turbulence driving conditions. In this study, we employ a novel, massively parallel hybrid code, HYPERS (Omelchenko & Karimabadi, 2012, 2021). The asynchronous model in HYPERS has recently been enhanced with a stretched mesh capability discussed in this study. This unique adaptivity makes HYPERS a natural choice for modeling multiscale space and laboratory plasmas. In particular, 3D HYPERS simulations of the lunar wake and the Earth's foreshock were found to be in a good agreement with observations (Omelchenko, Roytershtyen, et al., 2021).

The rest of the study is organized as follows. In Section 2, we overview the space-time adaptive HYPERS model and discuss a magnetospheric simulation setup adopted in this study. In Section 3, we present results from 3D simulations of solar wind interactions with the Earth's dayside magnetosphere under southward and northward quasi-radial IMF conditions. We compare our results to statistical data from observations and previous results from 2D simulations in Section 4. Key points of our investigation are summarized in Section 5.

2. HYPERS Model

2.1. Hybrid Equations

The HYPERS model implements a standard set of hybrid equations. It neglects the displacement current in Maxwell's equations, assumes a quasi-neutral fluid approximation for the inertialess plasma electrons, and treats all ion species as kinetic macro-particles with a PIC method (Omelchenko & Karimabadi, 2012):

$$\mathbf{E} = \frac{\mathbf{J}_e \times (\mathbf{B} + \mathbf{B}_{ext})}{en_e c} - \frac{\nabla p_e}{en_e} + \eta \mathbf{J}, \tag{1}$$

$$\nabla \times \mathbf{B} = \frac{4\pi}{c}\mathbf{J}, \mathbf{J} = \mathbf{J}_e + \mathbf{J}_i, \tag{2}$$

$$\frac{\partial \mathbf{B}}{\partial t} = -c\nabla \times \mathbf{E}, \tag{3}$$

$$en_e = \rho_i, \tag{4}$$

$$p_e = n_e T_e \sim n_e^{\gamma}. \tag{5}$$

In Equations 1–5 e is the absolute value of electron charge and c is the speed of light; n_e, $\mathbf{J}_e$ are the electron number and current density, respectively; p_e is the electron pressure, assumed to evolve adiabatically (see Equation 5) with the adiabatic constant, $\gamma = 5/3$; T_e is the electron temperature; ρ_i, $\mathbf{J}_i$ are the total ion charge and current density; $\mathbf{E}$, $\mathbf{B}$ are the self-generated electric and magnetic fields, respectively; $\mathbf{B}_{\text{ext}}$ is a static external magnetic field; η is the plasma resistivity.

In the simulations discussed in this study the density and current dependent plasma resistivity, η is represented as follows:

$$\eta = \eta_{ch} + \eta_v, \tag{6}$$

$$\eta_{ch} = \frac{4\pi\nu_{ch}}{\omega_{pe}^2}, \nu_{ch} = c_{ch}\omega_{pi}\left[1 - exp\left(-\frac{v_d}{3v_s}\right)\right], \tag{7}$$

$$\eta_v = \frac{4\pi\nu_v}{\omega_{pi}^2}, \nu_v = c_v\Omega_{ci}exp\left(-2n_e / n_{min}\right), \tag{8}$$

$$v_d = \left|\mathbf{J}\right| / en_e, v_s = \sqrt{\gamma T_e / m_i}, \tag{9}$$

where m_i is the ion (proton) mass, $n_{\min}$ is the minimum (cutoff) electron number density used in the hybrid model, and ω_{pe}, ω_{pi} are the electron and ion (proton) plasma frequencies, respectively. Ω_{ci} is the solar wind ion cyclotron frequency.

The Chodura resistivity, η_{ch} was previously used in 3D HYPERS simulations of field-reversed configurations (Omelchenko, 2015). The "vacuum" resistivity, η_v vanishes at cells occupied with plasma, $n_e \gg n_{\min}$. The resistivity and electron density cutoff values in our simulations are chosen to be small enough not to significantly alter the wave dispersion: $c_{ch} = 0.01$, $c_v = 0.5$, $n_{\min} = 0.1\ n_{\text{sw}}$, where n_{sw} is the number density of unperturbed solar wind. The "vacuum" cells, where $n_e \le n_{\min}$, may also be treated as pure "magnetic diffusion" cells by forcing the first two terms in the RHS of Equation 1 to vanish. The *ad hoc* resistivity in hybrid simulations emulates finite electron mass and radiation effects excluded from the standard hybrid model.

2.2. Magnetospheric Setup

Global 3D hybrid simulations of the Earth's magnetosphere are challenging even on modern parallel computers because of their highly inhomogeneous, disparate and dynamic time scales, ranging from fast

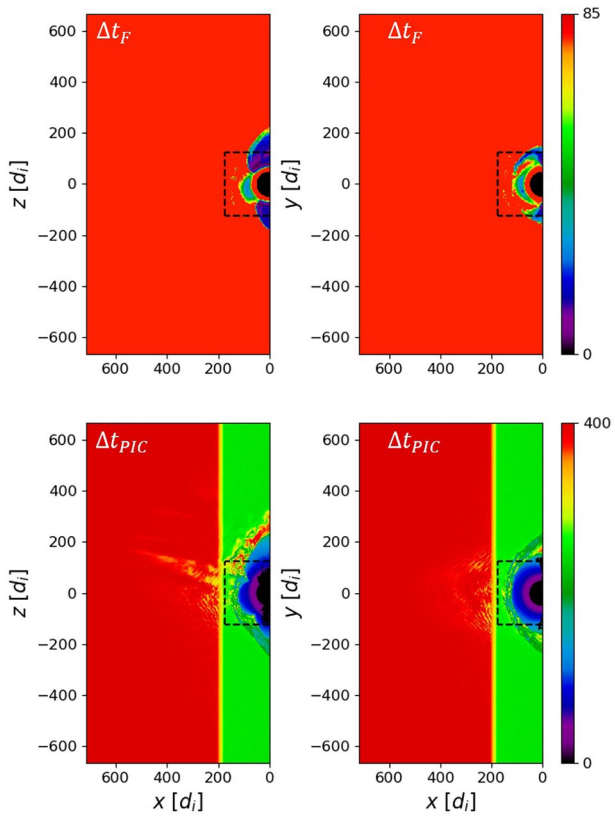

Figure 1. Southward interplanetary magnetic field, $\Omega_{ci}t = 269$: spatial distributions of field (top) and particle (bottom) time increments, normalized to $1/\omega_{pi}$, in the central *x*-*z* and *x*-*y* planes (geocentric solar magnetospheric coordinates). The dashed black line shows the boundary of the uniform patch.

whistler and ion gyro-scales to MHD scales. In order to accurately inject the solar wind plasma with a prescribed embedded IMF into the simulation domain, inflow and lateral domain boundaries should be positioned far enough from the magnetic dipole (when modeling the magnetotail, the outflow boundary should also be moved far away). Since in general hybrid simulations need to resolve spatial features of the order of the solar wind proton inertial length, d_i, the maximum size of a computational domain may be severely limited when covered with a uniform mesh. These spatial constraints are further exacerbated by ultra-fast time scales that typically arise in the near-Earth space. In time-stepped hybrid simulations these physical scales necessitate the use of very small time steps *everywhere* in the simulation domain. The failure to use sufficiently small time steps often leads to numerical instabilities (Omelchenko & Karimabadi, 2012). These instabilities may be difficult to mitigate without making the numerical plasma highly resistive, that is, without significantly altering the underlying hybrid model. Below we describe how these challenges are resolved in HYPERS.

Our magnetospheric simulations are set up in a rectangular Cartesian computational domain. The solar wind (proton) plasma is uniformly initialized with a drifting Maxwellian distribution everywhere except a spherical obstacle that models the Earth's ionosphere. The magnetic dipole is embedded at the obstacle center. Electromagnetic fields in Equations 1–5 are initialized as follows: $\mathbf{E} = \mathbf{B} = 0$, $\mathbf{B}_{\text{ext}} = \mathbf{B}_{\text{dip}} + \mathbf{B}_{\text{IMF}}$, where $\mathbf{B}_{\text{dip}}$, $\mathbf{B}_{\text{IMF}}$ are the magnetospheric (dipole) and interplanetary magnetic field, respectively. Throughout this study, if not stated otherwise, we present our results in the geocentric solar magnetospheric (GSM) coordinate system. It has its origin at the center of the Earth and its *x*-axis directed from the Earth to the Sun. The *y*-axis is defined to be perpendicular to the Earth's magnetic dipole so that the *x*-*z* plane contains the dipole axis. The positive *z*-axis points northward. The simulations, however, are performed on a uniform logical mesh defined in a simulation frame of reference. The axes in these two systems are oriented with respect to each other as follows: $(x,y,z)_{\text{GSM}} \rightarrow (-x,z,y)_{\text{sim}}$. Figures 1 and 2 below show distances in physical (GSM) and logical (code) coordinates, respectively.

The HYPERS model employs a modified formula for the dipole's magnetic field in three dimensions. Together with a scaled-down magnetic dipole moment, this modification enables a faster dropping of the dipole's field at larger distances for more accurate "far-field" boundary conditions. In this study, however, the stretched mesh achieves the same purpose. Therefore, this correction has been chosen to be small, as explained below. A modified dipole's vector potential, $\mathbf{A}_{\text{dip}}$ is written as a function of the position, $\mathbf{r}$ with respect to the dipole:

$$\mathbf{A}_{dip}(\mathbf{r}) = f(r)\frac{\mathbf{m} \times \hat{\mathbf{r}}}{r^2}, \tag{10}$$

where $\mathbf{m}$ is the magnetic dipole moment, $r = |\mathbf{r}|$, $\hat{\mathbf{r}} = \mathbf{r} / r$, and $f(r)$ is a differentiable function ($f(r) = 1$ corresponds to the standard dipole formula). Using Equation 10 the modified dipolar magnetic field, $\mathbf{B}_{\text{dip}} = \nabla \times \mathbf{A}_{\text{dip}}$ can be readily found:

$$\mathbf{B}_{dip}(\mathbf{r}) = \hat{\mathbf{r}}\left(\mathbf{m} \cdot \hat{\mathbf{r}}\right)\left[\frac{3f}{r^3} - \frac{f'}{r^2}\right] + \mathbf{m}\left[\frac{f'}{r^2} - \frac{f}{r^3}\right], \tag{11}$$

where $f' \equiv df/dr$. To make $\mathbf{B}_{\text{dip}}(\mathbf{r})$ fall off with r faster than in the standard dipole formula, we choose $f(r)$ as follows:

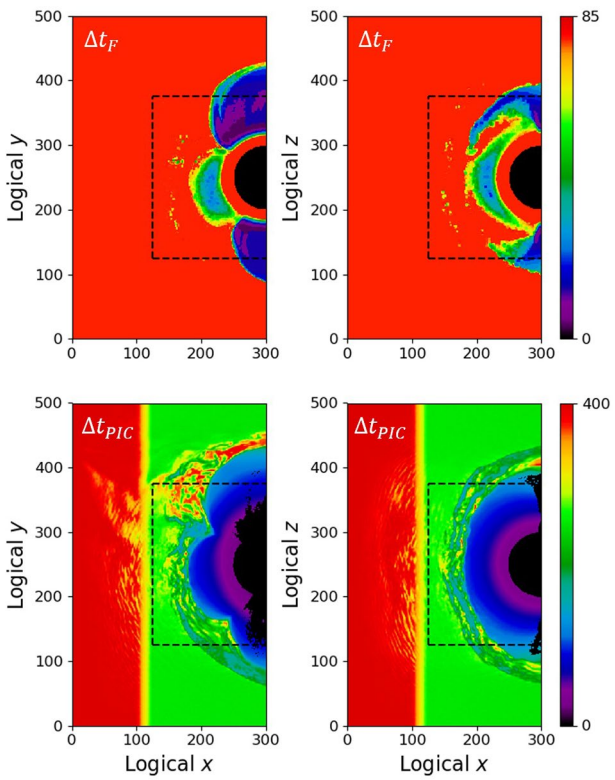

Figure 2. Southward interplanetary magnetic field, $\Omega_{ci}t = 269$: spatial distributions of field (top) and particle (bottom) time increments, normalized to $1/\omega_{pi}$, in the central logical *x-y* (geocentric solar magnetospheric [GSM] *x-z*) and *x-z* (GSM *x-y*) planes. The dashed black line shows the boundary of the uniform patch.

$$f(r) = exp\left[-\left(\frac{r}{r_{max}}\right)^4\right], \tag{12}$$

where $r_{\max}$ is a parameter such that $f \simeq 1$ for $r \ll r_{r\max}$.

We choose the obstacle radius, $R_{\text{obs}} = 50d_i \simeq 4R_E$, and assume a nominal magnetopause stand-off distance, $R_{M0} = 100d_i$. This distance is used to compute the magnetic dipole moment by balancing the solar wind dynamic pressure, $\rho_{sw}v_{sw}^2$ (ρ_{sw} and v_{sw} are the solar wind mass density and speed, respectively) with the characteristic magnetospheric field energy density, $B_m^2 / 8\pi$, where $B_m = |\mathbf{m}| / R_{M0}^3$. The simulation magnetopause distance in this study, $R_M \simeq 120d_i \simeq 10R_E$. We use $r_{\max} = 4.5R_{M0} = 450d_i$. Therefore, as already mentioned above, the dipolar field in our simulations is very close to the standard formula for all scales of interest.

The global simulation domain is composed of $300(x) \times 500(y) \times 500(z)$ cells. We define a uniform patch (box), $(125, 300)(x) \times (125, 375)(y) \times (125, 375)(z)$ in the logical coordinate system, corresponding to $(0, 175)(x) \times (-125, 125)(y) \times (-125, 125)(z)$ in the GSM coordinate system (in the units of d_i). The physical resolution inside the uniform patch is the same in all dimensions: $\Delta x = \Delta y = \Delta z = 1d_i$. Outside the uniform patch mesh cells are stretched towards simulation boundaries (see below). The total simulation volume is approximately $60 \times 110 \times 110R_E^3$. For comparison, if we had used a uniform spatial resolution everywhere, a global simulation volume would have been more than an order of magnitude smaller, $\sim 25 \times 40 \times 40R_E^3$.

In the simulations presented the obstacle is assumed to be particle absorbing and perfectly conducting. The perfectly conducting ionospheric response is valid for fast transient foreshock and magnetosheath phenomena studied here. In future simulations the spherical conductor may be assigned a finite conductivity in order to enable flux tube convection across the polar caps. We also initialize a dense immobile plasma with a characteristic radius, $R_c \simeq 1.1R_{\text{obs}}$ to model the cold plasmasphere.

At the inflow boundary a steady solar wind flow is specified to be injected in the $-x$-direction (GSM) with the same density, temperature, and velocity used to initialize the plasma. To damp reflected waves, "open field" conditions are implemented by introducing high-resistivity layers next to all domain boundaries. Outgoing solar wind particles escape through the outflow boundary. Backstreaming (sunward moving) particles are absorbed (removed from the simulation) prior to reaching boundaries inside their respective layers. Lateral boundaries reflect incoming (drifting Maxwellian) particles and absorb other particles.

2.3. Space Adaptivity

Previous HYPERS simulations were conducted on uniform meshes. Here, we present simulations performed on a logically uniform but physically stretched mesh. The stretched mesh enables use of larger and better resolved computational domains. In this study, the mesh is composed of a uniform box ("uniform patch"), which contains the obstacle, and the larger cells, stretched exponentially away from this patch towards simulation boundaries. The same maximum cell size growth factor of 12 is applied in all directions. The combination of mesh adaptivity with asynchronous computation (discussed below) results in a numerically robust and computationally efficient multiscale approach to global magnetospheric simulations.

For comparison, Figures 1 and 2 illustrate instantaneous time steps for particles and fields in the physical and logical coordinates, respectively. These Figures also show the uniform patch that we use for presenting simulation results.

Macro-particles are injected cellwise in the GSM $-x$ direction. Along the y and z directions mesh cells are initially assigned the same numbers of macro-particles, with particle weights being scaled proportionally to the physical cell size in the respective direction. In the x-direction, however, particle weights are not scaled. Instead, the number of particles at each cell is chosen to be proportional to the cell size in this direction. This choice of variable particle weights enables accurate injection and transport of the solar wind plasma on the stretched mesh. Particles are advanced and tested for entering the obstacle in the physical space, but initialized and saved for restarts in the logical space. Particle field interpolation and charge/current deposition on the mesh are performed in logical coordinates. In order to prevent non-physical oscillations that may develop at stretched cells with small resistivity values, we scale the plasma resistivity, η quadratically with respect to the cell size. The relationship between logical and physical coordinates in our simulations can be understood by comparing the corresponding physical features in Figure 1 (GSM coordinates) and Figure 2 (logical coordinates).

Previously, stretched spherical meshes were employed to conduct 2D (Lin, 2003) and 3D (Lin & Wang, 2005) hybrid simulations of the Earth's magnetosphere. A spherical mesh was also used in the hybrid simulations of solar wind interactions with planets like Venus by Dyadechkin et al. (2013). We note, however, that results from hybrid simulations, carried out on spherical and Cartesian meshes, may be somewhat different, as demonstrated by Dyadechkin et al. (2013). Therefore, to rule out potential geometric artifacts that may arise due to a stretched mesh, we performed a series of numerical tests and ascertained that there are no significant differences in results obtained on stretched and equivalent uniform meshes. For maximum fidelity, we employ a uniform patch in the near-Earth region.

2.4. Time Adaptivity

One of the notable HYPERS features is its time adaptivity. It is implemented using a general simulation technology, EMAPS (Omelchenko & Karimabadi, 2012, 2021). Event-driven Multi-Agent Planning System (EMAPS) greatly facilitates global simulations of the Earth's magnetosphere by enabling integration of particle trajectories and discrete fields on their own, self-adaptive timescales, computed as a function of the underlying local physics and mesh properties. Essentially, EMAPS is a “simulation time operating system” designed to advance in time local (cell scale) and global (model scale) physical quantities on an as-needed basis via discrete-event simulation with embedded elements of artificial intelligence. The asynchronous computation in HYPERS preserves flux conservation (Omelchenko & Karimabadi, 2006b, 2007) and $\nabla \mathbf{B} = 0$ (Omelchenko & Karimabadi, 2006a, 2012, 2021) down to the rounding precision. EMAPS enables computationally efficient, numerically stable and time accurate asynchronous advances of spatially coupled and (in general) temporally disparate computational elements, such as particles, mesh-based variables, external models, etc. The order of numerical updates is determined in a “game of life” fashion. In contrast, time-stepping techniques offer only restricted control over global time steps. The explicit algorithms in particular are known to undergo explosive numerical instabilities when facing disparate time scales, especially in strongly nonlinear regimes and under noisy conditions. This creates computational challenges for traditional hybrid simulations of solar wind interactions with the Earth's magnetosphere.

Figures 1 and 2 show instantaneous distributions of event-driven particle and field time steps. Adaptive time steps, generated “on the fly” by EMAPS, match constantly changing temporal dynamics in the simulation. Note that the larger particle time steps, shown in these Figures in the red color, are automatically selected to match the larger cell sizes in the x direction. These time steps, however, are restricted from above by gyro-frequency conditions (Omelchenko & Karimabadi, 2012) for better parallel efficiency.

HYPERS offers several parallel domain partitioning algorithms designed to allocate more processing power to computationally intense regions with finer mesh resolution and faster time scales. In general, the HYPERS computational domain can be decomposed into an arbitrary collection of contiguous rectangular boxes. In the simulations presented here, however, we employ a stretched parallel processor grid which roughly matches the contours of the underlying stretched mesh.

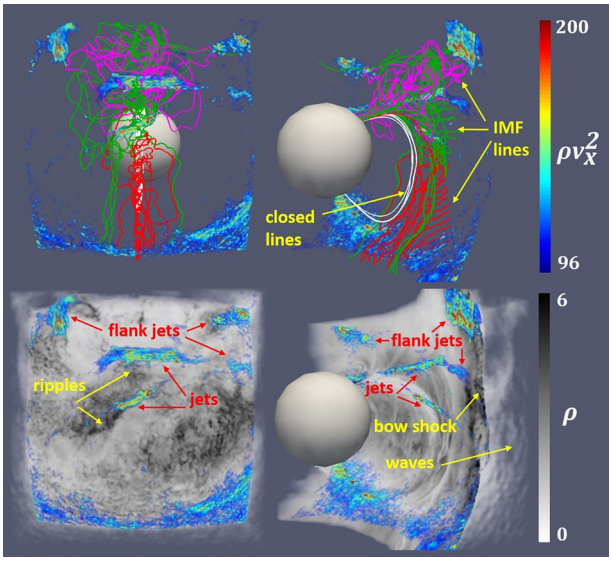

Figure 3. Southward interplanetary magnetic field, $\Omega_{ci}t = 269$: 3D plasma structures inside the uniform patch shown for two viewing angles. Top: magnetic field lines, colored according to their seed points, with embedded jets (ρv_x^2). Bottom: the volume rendered plasma density, ρ with embedded jets. For more detail refer to (Omelchenko, Chen, & Ng, 2021).

3. Simulation Results

We present results from two HYPERS simulations with the same IMF $B_x < 0$ component, one for southward IMF ($B_z < 0$) and one for northward IMF ($B_z > 0$). Both IMF conditions use the same absolute value of IMF cone angle, $\theta_{\rm IMF} = 10°$ in the GSM x-z plane with respect to the solar wind direction. The Earth's magnetic dipole is assumed to be in the summer position for the Northern Hemisphere, being tilted at 11.5° with respect to the GSM z-axis. The solar wind ions are represented by protons only.

All simulation quantities are presented below in the normalized form: the magnetic field components, B_x, B_y, and B_z and strength, $|\mathbf{B}|$ are normalized by the IMF strength, $B_{\rm IMF}$; the ion velocity, v by the characteristic Alfvén speed, v_A; the ion mass density, ρ by the upstream (solar wind) ion mass density, $\rho_{\rm sw}$; the ion temperature (thermal speed squared), T by v_A^2; the dynamic pressure, ρv_x^2 by $\rho_{sw} v_A^2$. The physical x, y, and z coordinates are normalized by the ion inertial length, d_i. The simulations are initialized with dimensionless solar wind parameters typical for quasi-radial IMF conditions: the Alfvén Mach number, $M_A = v_{\rm sw}/v_A = 8$; the ratio of the proton plasma frequency to the proton cyclotron frequency, $\omega_{pi}/\Omega_{ci} = 8{,}000$; and the ion and electron beta values, $\beta_i = \beta_e = 0.5$, respectively.

For convenience, we present data only from the uniform patch, where the mesh resolution is the highest. Color bars in all Figures use linear scales and therefore show only the minimum and maximum values of quantities represented. Text annotations in Figures facilitate their reading. Below we provide 2D (plane) and 1D (line) cuts through jet structures, which give detailed information about their physical properties and spatial scales. We also show 3D plots of jets (dynamic pressure), density perturbations and selected magnetic field lines. In addition, we provide a hyperlink to the data repository of 360° videos of these 3D configurations (Omelchenko, Chen, & Ng, 2021).

3.1. Southward IMF

Figure 3 reveals a 3D structure of the bow shock and magnetosheath in the southward IMF case for $\Omega_{ci}t = 269$ at two viewing angles (for a 360° view of this configuration see Omelchenko, Chen, & Ng, 2021). The top panels in this Figure illustrate selected closed and open magnetic field lines, the bottom panels show the corresponding plasma density plots. Field lines are color coded to facilitate their visual tracing in 3D: red and green lines are initiated in the IMF region from seed locations along a z-line ($x = 148$, $y = -0.5$) at $z < 0$ and $z > 0$, respectively; white lines are seeded close to the magnetopause inside a sphere of radius 4 centered at (116.7, −0.5, and −0.5); magenta lines are seeded inside a sphere of radius 35 centered at (131.9, −0.5, and 67.5). Importantly, this Figure elucidates the 3D topology of dynamic plasma pressure (ρv_x^2) structures rendered above a threshold factor, 1.5 with respect to the solar wind value, $\rho_{sw} v_{sw}^2$. We identify these structures as high-speed jets. The 3D plasma density plots also show the bow shock boundary, ripples and foreshock waves characteristic of quasi-radial IMF conditions.

Jets shown in Figure 3 have "pancake" shapes and durations of order $\sim$(10–25)Ω_{ci} ($\sim$30–75 s for $B_{\rm IMF} \simeq 3.5$ nT). Two jets cross the central meridional plane, being located at mid (smaller jet) and higher (larger jet) latitudes. Flank jets are also shown in this Figure. The approximate dimensions of the larger jet are $6R_E$ (width) $\times$ $4R_E$ (depth) $\times$ $0.6R_E$ (thickness), where "depth" measures jet extension into the magnetosheath, "width" is the characteristic jet scale in the equatorial plane, and "thickness" is the dimension that is appreciably shorter than the others. The size of the smaller jet is approximately $3R_E$ (width) $\times$ $2.5R_E$ (depth) $\times$ $0.6R_E$ (thickness). Both jets visually appear to be "wrapped" by quasi-radial magnetic field lines that penetrate into the magnetosheath: the larger jet is embedded in the magenta lines and the smaller one in the green lines. A closer look reveals that these entangled field lines connect the IMF region to the magnetosphere.

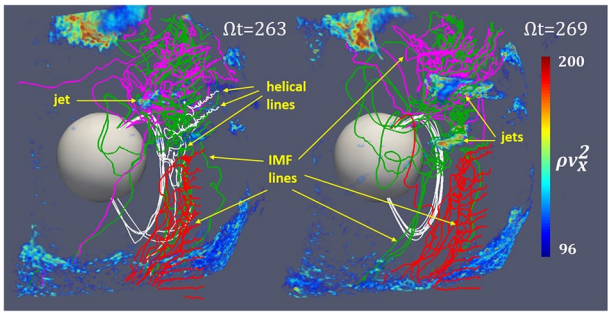

Figure 4. Southward interplanetary magnetic field: magnetic field lines, colored according to their seed points, with embedded jets (ρv_x^2) inside the uniform patch at two close moments in simulation time. Magnetopause reconnection signatures in the form of helical magnetic field lines at $\Omega_{ci}t = 263$ appear at mid latitudes almost simultaneously with the jets shown.

At this simulation moment ($\Omega_{ci}t = 269$) the white magnetic field lines, which originate near the magnetopause, appear to be slightly bent at mid-latitudes. A more detailed inspection, as shown in Figure 4, reveals multiple instances of magnetopause reconnection occurring a few moments earlier ($\Omega_{ci}t = 263$) in the form of white helical magnetic field lines aligned normal to the closed white meridional lines. The joint appearance of jets and reconnection signatures in our simulations may be indicative, as suggested by Karlsson et al. (2012), of a close physical connection between jets and magnetopause reconnection during periods of quasi-radial IMF, which is of general importance for solar wind-magnetosphere interaction studies. Based on our results, we conclude that these processes are more likely to represent concurrent, rather than sequential events.

Figure 5 presents the plasma density, dynamic pressure, temperature and magnetic field strength in the central meridional (GSM x-z) plane together with the projections of 3D magnetic field lines onto this plane. Note that in this case all lines that originate in the solar wind are colored in red. The magnetosheath in our simulations is extremely turbulent under the specified quasi-radial IMF conditions. The rippled bow shock surface "breathes" in time and space, often reaching the sunward boundary of the uniform patch, making the transition between the foreshock and bow shock uncertain to a significant degree on average. The sporadic formation of high-speed jets occurs in this transitional region, where IMF lines get entangled with open field lines of magnetospheric origin so that the incoming solar wind plasma is compressed, being "funneled" into the magnetosheath. Although the turbulence spatial scales may be somewhat exaggerated because of the downscaled size of the bow shock, our simulations capture the important kinetic physics of shock reformation and concomitant turbulent convection of magnetic field lines. Detailed characteristics of this turbulence will be discussed in a separate publication.

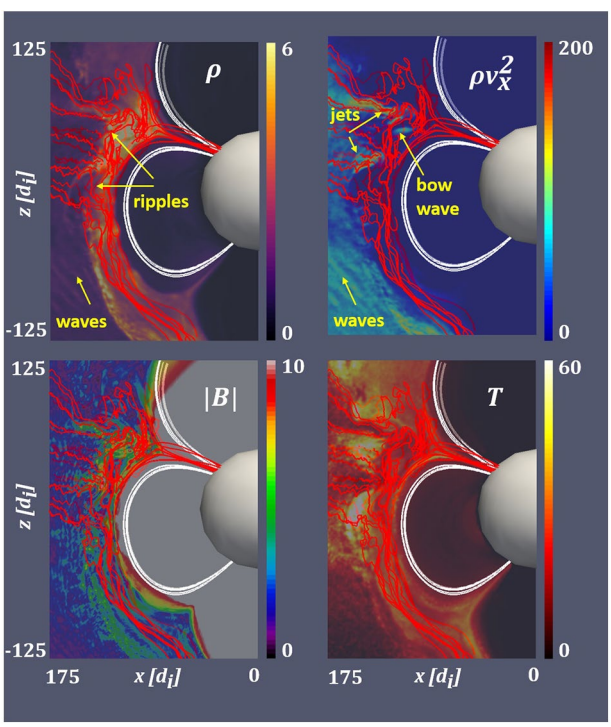

Figure 5. Southward interplanetary magnetic field, $\Omega_{ci}t = 269$: a central 2D cut ($y = 0$) in the uniform patch (geocentric solar magnetospheric coordinates). Left to right, top to bottom shown are: the plasma density, ρ, dynamic pressure, ρv_x^2, magnetic field strength, $|\mathbf{B}|$, and ion temperature, T. Red magnetic field lines are seeded in the solar wind, white lines are seeded on the obstacle surface.

One can see in Figure 5 that quasi-radial IMF lines, being entangled with magnetospheric field lines, terminate on the inner boundary in the northern cusp region. This configuration of magnetic field lines occurs sporadically, driven by the magnetosheath turbulence. The plasma density (ρ) panel clearly demonstrates the formation of plasma filaments with enhanced density that correlate well with the corresponding enhancements in the dynamic plasma pressure (ρv_x^2) and magnetic field strength ($|\mathbf{B}|$). At the same time these density filaments anti-correlate with the ion temperature drops (T). This suggests that jets are composed of compressed solar wind plasma. The corresponding Figure 6 shows the variation of the same physical quantities in a cross-sectional (y-z) plane.

The dynamic pressure panel of Figure 5 reveals a bow wave forming ahead of the larger jet. This wave can be seen more clearly in Figure 7. As also seen in the density panel of Figure 5, this particular moment in simulation time features a significant plasma density build-up in the northern part of the magnetosheath associated with the impact of the larger jet on the cusp. In a separate publication we will discuss how this density build-up leads to the precipitation of energetic ions into the cusp along the entangled magnetic field lines.

Figures 7 and 8 demonstrate the properties of two jets along their "depth" directions in the central meridional plane. The jets are seen to be composed of strongly compressed (by a factor of 3–5), locally super-Alfvénic ($M_A \simeq 5$) plasma. They propagate predominantly in the solar wind ($-x$) direction ($v_y \simeq 0$, $v_z \simeq 0$), gradually slowing down towards the magnetopause.

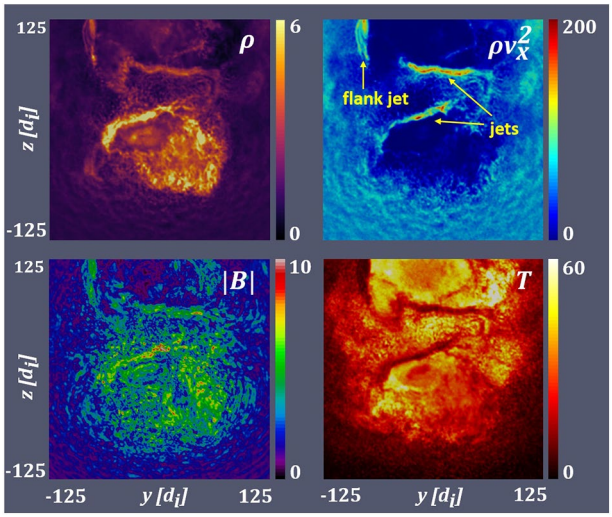

Figure 6. Southward interplanetary magnetic field, $\Omega_{ci}t = 269$: a 2D cut ($x = 138$) in the uniform patch (geocentric solar magnetospheric coordinates). Left to right, top to bottom shown are: the plasma density, ρ, dynamic pressure, ρv_x^2, magnetic field strength, $|\mathbf{B}|$, and ion temperature, T.

3.2. Northward IMF

Figure 9 illustrates a 3D structure of the bow shock and magnetosheath region in the northward IMF case for $\Omega_{ci}t = 406$ at two viewing angles (for a 360° view of this configuration see Omelchenko, Chen, & Ng, 2021). As in the southward IMF case, it shows the 3D topology of selected magnetic field lines, along with volume rendered density and dynamic pressure distributions for two viewing angles. The plasma density plot exhibits turbulent bow shock ripples and foreshock waves typical of quasi-parallel IMF conditions. This Figure also highlights a high-speed jet that impacts the magnetopause at a mid-southern latitude. This jet has an "arched pancake" shape, compared to "flat pancake" shapes discussed in the southward IMF case. The characteristic size of this jet is $4R_E$ (width) x $1.5R_E$ (depth) x $0.6R_E$ (thickness).

Magnetic field lines in Figure 9 are color coded by selecting line seed points as follows: red ($z < 0$) and green ($z > 0$) lines are seeded in the IMF region along a z-line ($x = 158$, $y = -0.5$). White closed lines are seeded close to the magnetopause inside a sphere of radius 5 centered at (118.3, −0.5, and −8.6). Magenta and cyan lines are seeded close to the jet inside a sphere of radius 20 centered at (133, 10.5, −51.9) and a sphere of radius 14.9 centered at (129, 35.1, and −69.5). In addition, open polar (white) lines are seeded in spheres of radius 4 near the southern pole at (37.2, 0.3, and −95.6) and the northern pole at (49, −1, and 63.2).

The highlighted jet is "wrapped" in a "knot" of magnetic field lines, which start in the solar wind as IMF lines and connect to the inner boundary surface near the north pole. The cyan, red and magenta lines, starting at mid-southern latitudes and terminating on the inner boundary near the north pole, are indicative of the existence of a non-local mechanism for energetic plasma transport from the magnetosheath into the northern cusp. The enhanced plasma flux is observed in the right ρ panel of Figure 9 in the form of a high density (dark color) streak near the north pole. This mechanism will be further discussed elsewhere. Importantly, this high-speed jet produces a strong impact on the magnetopause. This is visibly manifested as a "dent" in the closed (white) lines.

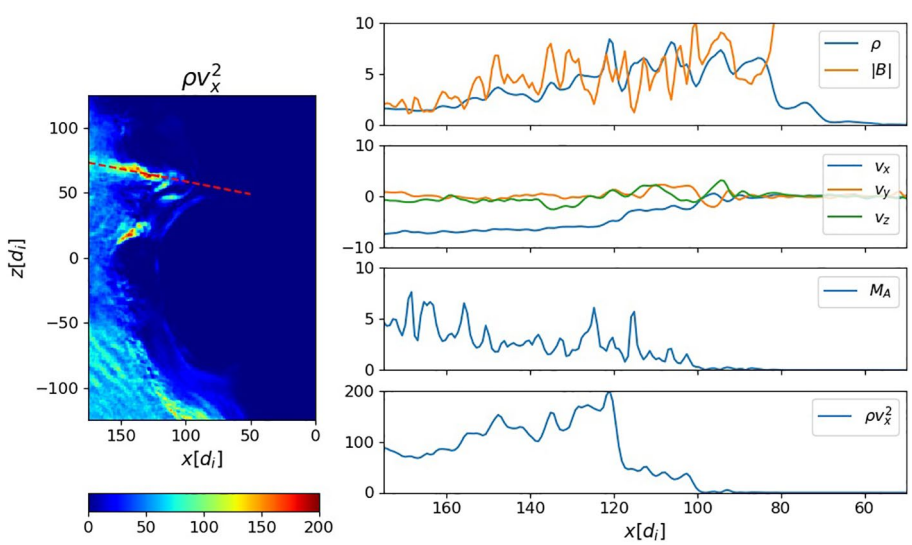

Figure 7. Southward interplanetary magnetic field, $\Omega_{ci}t = 269$. Left: a line cut (dashed red) along the upper jet in the central x-z plane (geocentric solar magnetospheric coordinates). Right: top to bottom shown are the profiles of plasma density, ρ and magnetic field strength, $|\mathbf{B}|$, plasma velocity components, v_x, v_y, and v_z, Alfvén Mach number, M_A, dynamic pressure, ρv_x^2 along the line.

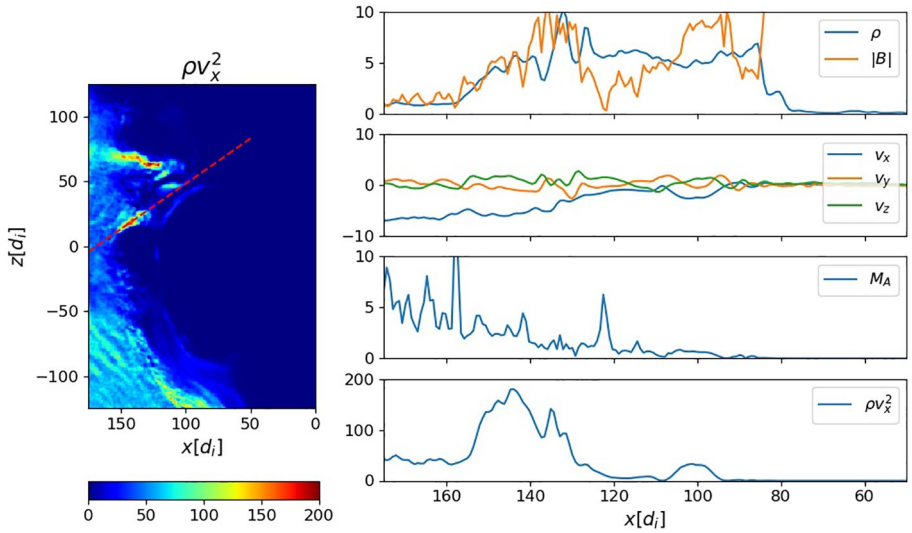

Figure 8. Southward interplanetary magnetic field, $\Omega_{ci}t = 269$. Left: a line cut (dashed red) along the lower jet in the central x-z plane (geocentric solar magnetospheric coordinates). Right: top to bottom shown are the profiles of plasma density, ρ, and magnetic field strength, $|\mathbf{B}|$, plasma velocity components, v_x, v_y, and v_z, Alfvén Mach number, M_A, dynamic pressure, ρv_x^2 along the line.

More jet details are illustrated in a 2D central meridional plane in Figure 10. As in the southward IMF case, this Figure juxtaposes selected magnetic field lines (seeded in the solar wind and colored in red) with the plasma density, ρ, dynamic pressure, ρv_x^2, magnetic field strength, $|\mathbf{B}|$ and ion temperature, T. The dynamic pressure enhancement correlates well with the corresponding density and magnetic field strength enhancements and anti-correlates with the reduced ion temperature.

The jet interaction with the magnetopause, featured in Figure 10, can also be seen in Figure 9. The jet is mostly aligned with the surrounding magnetic field lines. These field lines are sporadically drawn closer towards the magnetopause by the magnetosheath turbulence, visually manifested in the form of density ripples appearing at the bow shock front. One-dimensional jet profiles are shown in Figure 11. Similarly to the two jets considered in the southward IMF case, this jet represents the compressed (by approximately a factor of 5) solar wind plasma moving primarily in the $-x$-direction ($v_y \simeq 0$, $v_z \simeq 0$). The jet abruptly brakes near $x \simeq 120$ as it reaches the stronger dipole field at the magnetopause.

Finally, Figure 12 shows 2D profiles of the axial plasma velocity component, v_x. This Figure illustrates the early dynamics (left) and relaxation (right) of the magnetopause following the jet impact. The dark color in this Figure is indicative of the characteristic solar wind speed. The red colored regions around the magnetopause reveal localized sunward plasma flows ($v_x > 0$) that develop following the return of the magnetopause to its unperturbed position. Being generated near the location of the jet impact, these sunward flows spread beyond the original magnetopause position.

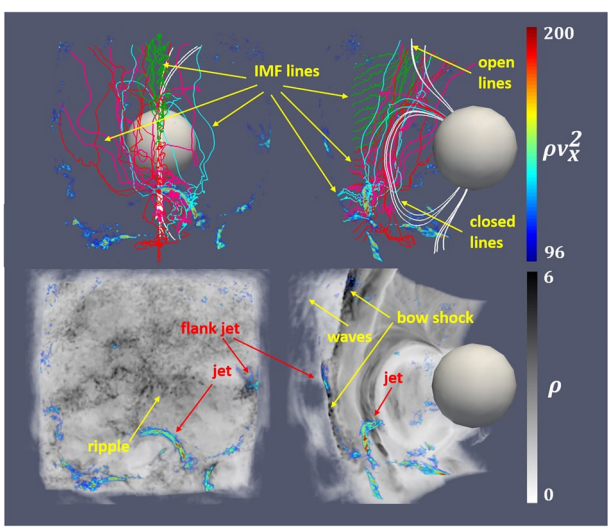

Figure 9. Northward interplanetary magnetic field, $\Omega_{ci}t = 406$: 3D plasma structures inside the uniform patch for two viewing angles. Top: magnetic field lines, colored according to their seed points, with embedded jets (ρv_x^2). Bottom: the volume rendered plasma density, ρ with embedded jets. For more detail refer to (Omelchenko, Chen, & Ng, 2021).

4. Discussion

4.1. Comparison With Observations

The 3D morphology and aspect ratios of magnetosheath jets observed by satellites have long been under debate. Observationally, Plaschke et al. (2020) and Palmroth et al. (2021) have recently reported significantly

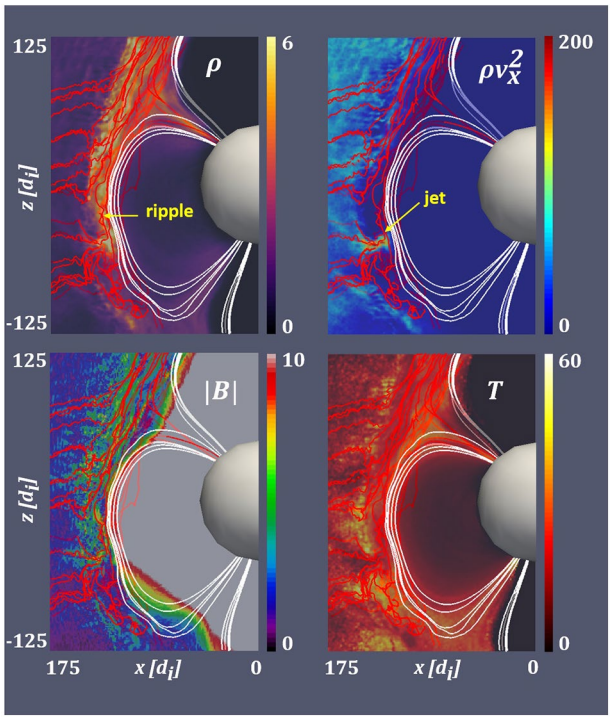

Figure 10. Northward interplanetary magnetic field, $\Omega_{ci}t = 406$: a central 2D cut ($y = 0$) in the uniform patch (geocentric solar magnetospheric coordinates). Left to right, top to bottom shown are: the plasma density, ρ, dynamic pressure, ρv_x^2, magnetic field strength, $|\mathbf{B}|$, and ion temperature, T. Red magnetic field lines are seeded in the solar wind, white lines are seeded on the obstacle surface.

smaller characteristic sizes for magnetosheath jets using THEMIS and Magnetospheric Multiscale (MMS) data, respectively. The typical jet scales have been estimated to be below $\sim 0.2R_E$, approximately one order of magnitude smaller than previously reported. Plaschke et al. (2020), however, point out that larger jets are also observed, albeit not as frequently. In our simulations small jets form far more frequently than large jets discussed above, which is consistent with these statistical inferences. In this study, however, we discuss only large jets, with the most significant impact on the magnetosphere. For instance, according to Vuorinen et al. (2019) 5–60 large jets (with sizes exceeding $1R_E$) per hour impact the subsolar magnetopause. Below, we compare dimensions and properties of these jets to satellite data inferred from a broad range of observations mostly made under steady quasi-radial IMF conditions similar to ones adopted in our simulations. Further statistical analysis of jet occurrences and size distributions is left for future, better resolved and longer simulations.

Dmitriev and Suvorova (2015), for instance, report a well-developed jet with the size $\sim 2R_E$ and duration from 70 to 80 s, with an initial speed of 380 km/s close to the unperturbed solar wind speed, 400 km/s. They also observe the gradual slowing down of this jet to ~320 km/s while it was approaching the magnetopause. Based on statistical studies they estimate typical jet scales of the order of $(2–8)R_E$. Hietala et al. (2012, 2009) reported jet sizes perpendicular to the ambient magnetic field at least $\sim 1R_E$. We note that these jet characteristics (temporal scales, spatial sizes, and speeds) are consistent with the simulation jets presented in Section 3.

The investigation by Karlsson et al. (2012) revealed the existence of localized density enhancements of over 100% with scale sizes of the order of $(0.1–10)R_E$, with the dimension normal to the background magnetic field being substantially shorter than the others ($\sim 0.2R_E$). They concluded that jets have the form of pancakes ("flattened flux tubes"). They also found that the orientation of these plasmoids was such that the shortest scale tended to be parallel to the magnetopause normal.

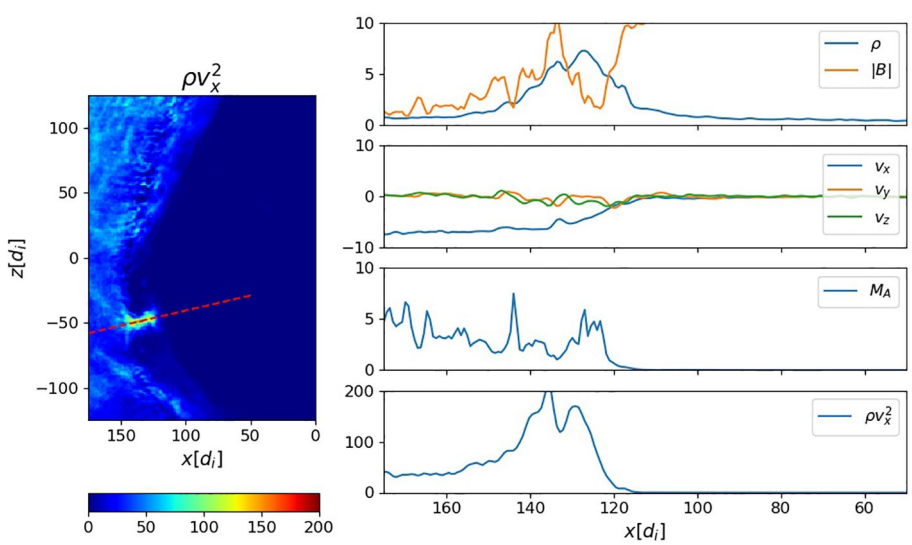

Figure 11. Northward interplanetary magnetic field, $\Omega_{ci}t = 406$. Left: a line cut (dashed red) along the jet in the central x-z plane (geocentric solar magnetospheric coordinates). Right: top to bottom shown are the profiles of plasma density, ρ and magnetic field strength, $|\mathbf{B}|$, plasma velocity components, v_x, v_y, and v_z, Alfvén Mach number, M_A, dynamic pressure, ρv_x^2 along the line.

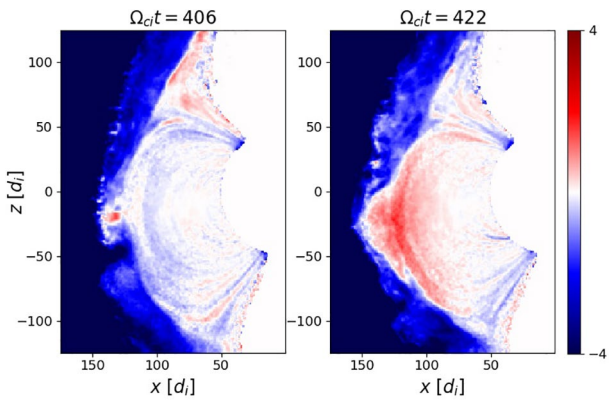

Figure 12. Northward interplanetary magnetic field: the plasma velocity component, v_x in the central x-z plane (geocentric solar magnetospheric coordinates) for two moments in simulation time. Sunward flows (red) in the subsolar region result from the magnetopause rebound after the impact of a high-speed jet.

Our simulations confirm that 3D jets have pancake shapes similar to those shown by Karlsson et al. (2012). We also note that their orientation with respect to the background magnetic field may vary, as demonstrated in the previous Section. Indeed, the magnetic field topology around jets (see Figures 3 and 9) may be complex since jets tend to be surrounded by entangled magnetic field lines. Therefore, using the ambient magnetic field as a reference for characterizing the 3D jet topology in observations may lead to somewhat ambiguous results. This may also explain a wide range of possible jet shapes inferred from different observations (Plaschke et al., 2018).

We further note that Archer et al. (2012) found the spatial dimensions of magnetosheath dynamic pressure enhancements to be of the order of $\sim 1R_E$ parallel to the flow and $\sim(0.2\text{–}0.5)R_E$ in the perpendicular direction. They, however, presumed that at least some of these pulses might be caused by solar wind discontinuities interacting with the bow shock, which is beyond the focus of this study, which assumes steady IMF conditions.

Karlsson et al. (2012) found that density enhancements in jets are generally elongated along the ambient magnetic field. The simulation jets in this study are generally consistent with these observations (however, as noted above, the ambient magnetic field may be complex). Karlsson et al. (2015) also noted that the minimum plasmoid size (i.e., the minimum density variance direction) does not necessarily coincide with the direction of flow velocity. This means that jets are generally observed as high-speed plasmoids of pancake shapes tilted with respect to their flow velocity. This is also consistent with our findings (see Figures 3, 5, 6, 9 and 10). We note that 3D simulations are essential for accurately capturing the magnetic topology of jets. Karlsson et al. (2012) concluded that the tendency of these plasmoids to orient themselves with respect to the magnetopause "quite far out in the magnetosheath" points out to either their local generation, or a modification of structures preexisting in the pristine solar wind. Our simulations suggest a local mechanism for jet generation through compression and transport of solar wind plasma by entangled magnetic field lines which sporadically form in the turbulent magnetosheath.

As discussed by Plaschke et al. (2018), MMS data provide additional insight into the structure of jets and associated current sheets. In particular, the jets are associated with enhancements in current density. Our simulations confirm these findings. Although we do not present these distributions here, the approximate scales of current sheet boundaries ($|\mathbf{B}|$ gradient scales) of the order of a few d_i can be inferred from $|\mathbf{B}|$ plots shown in Figures 5, 6 and 10.

The question of relative contributions of density and velocity to the increase in dynamic pressure and change in magnetic field strength, as inferred from different observations, remains controversial as observations point out to a continuum of various relative density/velocity contributions and magnetic field responses (Plaschke et al., 2018). This controversy may be a result of different statistical approaches adopted across a wide range of isolated studies and different jet locations across the magnetosheath (e.g., central vs. flank locations). We note, however, that on average statistical distributions of changes in magnetic field strength and density associated with jets have maxima corresponding to their enhancements (Plaschke et al., 2018). The simulation jets discussed in Section 3 are unambiguously characterized by density and magnetic field strength enhancements. This is consistent with results reported by Hietala et al. (2012, 2009), as well as evidence that jets with density enhancements greater than 40% are almost exclusively associated with magnetic field strength enhancements (Archer & Horbury, 2013).

A much better agreement is found in statistical studies of ion temperatures in jets with respect to the background magnetosheath temperature. The statistical study by Plaschke et al. (2013) found that both the perpendicular and parallel temperatures are reduced in jets compared to the respective magnetosheath temperatures. Archer and Horbury (2013) also confirm that jets associated with density enhancements always have reduced ion temperatures. These observational data are consistent with our results shown in

Figures 5, 6 and 10. These results suggest that simulation jets represent compressed solar wind plasmoids with velocity and temperature characteristics close to those of pristine solar wind. This conclusion is also consistent with many reports that jets, despite their generally oblique orientations, have a tendency to propagate straight along the Sun-Earth line in the background magnetosheath flow (Archer & Horbury, 2013; Hietala & Plaschke, 2013; Hietala et al., 2012). The dominance of the v_x component over other velocity components in the simulated jets, as shown in Figures 7, 8 and 11, confirms this observational evidence. These Figures also identify simulation jets as super-Alfvénic in the $-x$-direction, which is also confirmed by observations (Plaschke et al., 2013).

We further note that observational jets with density decreases have speeds close to the Alfvén speed, which is typical of Flux Transfer Events (Archer & Horbury, 2013). This subset of magnetosheath jets, associated with the subsolar magnetopause, is also characterized with enhanced temperatures (Archer & Horbury, 2013). All these properties clearly differentiate that particular type of jets from the jets discussed in our study.

Long-lived high-speed jets may form local bow waves, which are also detected in our simulations (see the upper jet in Figure 5). These bow waves present significant interest as sites of turbulence-driven particle acceleration and magnetosheath heating (Liu et al., 2019). Inward magnetopause motion and large sunward flow velocities in observations are frequently associated with jets that directly impact the magnetopause (Hietala et al., 2012, 2009). Figure 10 demonstrates a high-speed jet that directly terminates on the magnetopause. We also demonstrate sunward flows generated during a rebound of magnetopause location in Figure 12.

4.2. Comparison With 2D Simulations

Well-resolved structures of enhanced dynamic plasma pressure, identified as magnetosheath jets, were demonstrated by Karimabadi et al. (2014) in 2D hybrid simulations of the dayside magnetosphere under quasi-radial IMF conditions. More recently, 2D hybrid simulations of spontaneous flow anomalies by Omidi et al. (2016) emphasized regions of enhanced flow speed near the bow shock, reminiscent of high-speed jets. The 2D geometry, however, describes a cylindrical Earth with an ever-expanding magnetosphere. This setup introduces an artificial topology of magnetic field lines, which affects the structure of turbulent magnetosheath in global hybrid simulations. For instance, 2D simulations performed by Karimabadi et al. (2014) at high Mach numbers (~8–10) produce patterns of long, serpentine (bent and deflected) structures of enhanced dynamic pressure, which cannot be reconciled with the observations (Plaschke et al., 2018).

The results from the high-resolution simulations by Karimabadi et al. (2014) seem to run counter to a report by Omidi et al. (2016) that 2D jets become less structurally coherent at high solar wind Mach numbers. Omidi et al. (2016), however, do not provide dynamic pressure snapshots. This makes further comparison between these two 2D hybrid simulations difficult. Omidi et al. (2016) also report regions of high dynamic pressure associated with magnetosheath filamentary structures that penetrate the magnetosheath close to the magnetopause. They note, however, that these regions are not associated with high flow speeds, and therefore cannot be classified as high-speed jets.

Our 3D simulations predict transient compact jets, in full agreement with the observations. The 3D simulations further confirm the formation of super-Alfvénic bow waves ahead of jets (see one forming ahead of the larger jet in the ρv_x^2 panel in Figure 5) and anomalous sunward flows due to the impact of jets on the magnetopause (Figure 12). These features were first demonstrated by Karimabadi et al. (2014) in 2D. In the 3D simulations, however, bow waves have more compact shapes compared to those in 2D. Statistical properties of bow waves observed by satellites are discussed in a recent study by Liu et al. (2020).

In our simulations, we do not detect large-scale magnetosheath vortices driven by 2D jets, as shown by Karimabadi et al. (2014). This may be due to either the fundamental differences between 2D and 3D, or a lack of spatial resolution in our current 3D simulations compared to the 2D simulations in question. Importantly, the 3D simulations confirm findings by Karimabadi et al. (2014) that high-speed jets exhibit

enhanced magnetic field strengths, lower temperatures and higher densities compared to the ambient (magnetosheath) plasma.

It should also be noted that Karimabadi et al. (2014) refer to the solar wind flow deflection by bow shock surface ripples, as suggested by Hietala et al. (2012, 2009). However, our analysis points out a different mechanism for jet origin whereby the jet formation is tied to the turbulent dynamics of magnetic field perturbations. The ion kinetic effects in this mechanism are essential as they play a key role in controlling turbulent shock reformation under quasi-radial IMF conditions. The origin of jets in simulations by Karimabadi et al. (2014) seems to be similar in nature, albeit that spatio-temporal characteristics of turbulence in 2D simulations are very different. Therefore the geometric properties of 2D jets are different too.

More recently, 2D global hybrid-Vlasov simulations of magnetosheath jets have been performed with the Vlasiator code using magnetic dipoles with unscaled strengths and mesh resolutions of the order of the proton inertial length (Palmroth et al., 2018, 2021). These simulations generated many small-size jets but none as large as found in the hybrid-PIC simulations. There are a number of factors that may contribute to this difference in simulation results. First, similarly to the 2D hybrid simulations discussed above, the Vlasiator simulations model a cylindrical magnetosphere which produces turbulent patterns in the magnetosheath different from those forming in three dimensions. Second, jet simulations may be sensitive to input parameters like solar wind plasma properties, IMF strength/orientation and dipole tilt. For instance, we see significant differences in transient plasma features in the southward and northward IMF cases. In the future, we plan to conduct further studies of jets by capitalizing on the new adaptive capabilities of HYPERS.

4.3. Jet Origin

In Section 3, we have demonstrated the generation and impact of high-speed 3D magnetosheath jets on the cusp and magnetopause under steady quasi-radial southward and northward IMF conditions. The origin of jets is still being debated. For instance, as was mentioned in Section 1, it was suggested by Hietala et al. (2012, 2009) that jets may be generated due to the downstream convergence of solar wind flows deflected by oblique plasma ripples which naturally form during turbulent self-reformation of quasi-parallel shocks. The connection between the observed jets and bow shock ripples was statistically confirmed by Hietala and Plaschke (2013). In Section 3, we have shown, however, that in our simulations jets naturally arise as high-density solar wind plasma structures associated with magnetic field filaments, which dynamically emerge during the turbulent motion of magnetosheath plasma. Although we also confirm the existence of bow shock ripples, we must emphasize a principal difference between these two different interpretations of jet origin.

In the "ripple theory" by Hietala et al. (2009, 2012) high-speed jets are assumed to form due to the shock front deflection and downstream convergence of upstream solar wind plasma.

The jets shown in Figures 5 and 10 do not appear directly behind the rippled shock front. We conclude that the origin of these jets is closely tied to the turbulent dynamics of the magnetic field. The turbulent process of shock reformation develops in the magnetosheath under quasi-radial IMF conditions due to the ion kinetic effects and therefore is not magnetohydrodynamic in nature.

The movement of magnetic field and concomitant density perturbations in the magnetosheath constitutes the turbulence driven by the solar wind flow. The magnetic field perturbations lead to the compression of the incoming solar wind plasma, which is ultimately manifested in the form of local enhancements of plasma dynamic pressure, identified as high-speed jets. These plasma structures naturally have low temperatures compared to the magnetosheath plasma and travel at velocities close to one of unperturbed solar wind. In some cases they may penetrate deep into the magnetosheath, all the way to the magnetopause.

In Section 3, we have analyzed three jets selected to demonstrate the impact of large (Earth-size) jets on the cusp and the magnetopause. Similar structures, as can be seen, for instance, in Figure 3, may appear on the flanks of the magnetosheath. Smaller jets also sporadically emerge in our simulations.

Interestingly, while discussing possible mechanisms for jet generation, Raptis et al. (2020) note that although "it seems that jet generation could be related to the ripples of the bow shock, there could be more

factors that influence their generation that may or may not be connected to this mechanism." They further note that the IMF frozen into the solar wind may have "a more important impact on the jets than previously thought." Our simulations provide strong evidence in support of this point of view since they point out a "magnetokinetic" mechanism whereby turbulent, entangled magnetic field lines control the compression of solar wind plasma and its penetration into the magnetosheath in the form of high-speed jets.

5. Summary and Conclusions

We have presented results from two 3D hybrid simulations of high-Mach solar wind interactions with the Earth's dayside magnetosphere, performed under steady southward and northward quasi-radial IMF conditions. These simulations, carried out with a novel, space-time adaptive hybrid code, HYPERS, have demonstrated the spontaneous generation of localized transient structures of enhanced dynamic plasma pressure in the magnetosheath, known as high-speed jets.

In the analysis of these simulations we have made an effort to address a number of outstanding science questions concerning the origin and properties of these jets. We conclude that these compact dynamic plasma pressure structures arise due to the turbulent convection of entangled field lines of IMF and magnetospheric origin, which sporadically form in the magnetosheath and create conditions favorable for compression of the solar wind plasma and its further penetration into the magnetosheath. This "magnetokinetic" process of jet formation is different from the "ripple theory" previously suggested by Hietala et al. (2009, 2012).

Our simulations have revealed 3D pancake-like dynamic pressure structures of jets, generally consistent with the observations. We have also confirmed other characteristics of jets such as densities, magnetic field strengths, temperatures, velocities, Alfvénic Mach numbers, and lifetimes, derived from observations. We have demonstrated that in some cases large high-speed jets can significantly impact the cusp and the magnetopause regions. This makes magnetosheath jets a key factor to consider in the overall theory of solar wind-magnetosphere-ionosphere interactions.

Data Availability Statement

Simulation data for this study are available at public data repositories (Omelchenko et al., 2020; Omelchenko, Chen, & Ng, 2021).

Acknowledgments
This material is based upon work supported by the National Aeronautics and Space Administration under grant 80NSSC19K0838 and grant NN-H16ZDA001N-HSR. The simulations presented in this study were performed on 12,800 parallel Ivy Bridge E5-2680v2 (2.8 GHz) processors of the Pleiades computer at the NASA Advanced Supercomputing facility at NASA's Ames Research Center. Each simulation run took ~20 h of wall clock time to complete. The authors thank Johnny Chang and Michael Heinsohn for their expertise in assisting this computational project. Y. Omelchenko acknowledges his fruitful discussions with H. Hietala, Vadim Roytershteyn, and T. Liu.

References

Archer, M. O., & Horbury, T. S. (2013). Magnetosheath dynamic pressure enhancements: Occurrence and typical properties. *Annales Geophysicae*, *31*, 319–331. https://doi.org/10.5194/angeo-31-319-2013

Archer, M. O., Horbury, T. S., & Eastwood, J. P. (2012). Magnetosheath pressure pulses: Generation downstream of the bow shock from solar wind discontinuities. *Journal of Geophysical Research*, *117*, A05228. https://doi.org/10.1029/2011JA017468

Dmitriev, A. V., & Suvorova, A. V. (2015). Large-scale jets in the magnetosheath and plasma penetration across the magnetopause: THEMIS observations. *Journal of Geophysical Research: Space Physics*, *120*, 4423–4437. https://doi.org/10.1002/2014JA020953

Dyadechkin, S., Kallio, E., & Jarvinen, R. (2013). A new 3-D spherical hybrid model for solar wind interaction studies. *Journal of Geophysical Research: Space Physics*, *118*, 5157–5168. https://doi.org/10.1002/jgra.50497

Hietala, H., & Plaschke, F. (2013). On the generation of magnetosheath high-speed jets by bow shock ripples. *Journal of Geophysical Research: Space Physics*, *118*, 7237–7245. https://doi.org/10.1002/2013JA019172

Hietala, N., Laitinen, T. V., Clausen, L. B. N., Facskó, G., Vaivads, A., Lucek, E. A., et al. (2012). Supermagnetosonic subsolar magnetosheath jets and their effects: From the solar wind to the ionospheric convection. *Annales Geophysicae*, *30*, 33–48. https://doi.org/10.5194/angeo-30-33-2012

Hietala, V., Andréeová, K., Vainio, R., Vaivads, A., Palmroth, M., Rème, H., et al. (2009). Supermagnetosonic jets behind a collisionless quasiparallel shock. *Physical Review Letters*, *103*, 245001. https://doi.org/10.1103/PhysRevLett.103.245001

Karimabadi, H., Roytershteyn, V., Vu, H. X., Omelchenko, Y. A., Scudder, J., Daughton, W., et al. (2014). The link between shocks, turbulence, and magnetic reconnection in collisionless plasmas. *Physics of Plasmas*, *21*, 062308. https://doi.org/10.1063/1.4882875

Karlsson, T., Brenning, N., Nilsson, H., Trotignon, J.-G., Vallières, X., & Facsko, G. (2012). Localized density enhancements in the magnetosheath: Three-dimensional morphology and possible importance for impulsive penetration. *Journal of Geophysical Research*, *117*, A03227. https://doi.org/10.1029/2011JA017059

Karlsson, T., Kullen, A., Liljeblad, E., Brenning, N., Nilsson, H., Gunell, H., & Hamrin, M. (2015). On the origin of magnetosheath plasmoids and their relation to magnetosheath jets. *Journal of Geophysical Research: Space Science*, *120*, 7390–7403. https://doi.org/10.1002/2015JA021487

Lin, Y. (2003). Global-scale simulation of foreshock structures at the quasi-parallel bow shock. *Journal of Geophysical Research*, *108*(A11), 1390. https://doi.org/10.1029/2003JA009991

Lin, Y., & Wang, X. Y. (2005). Three-dimensional global hybrid simulation of dayside dynamics associated with the quasi-parallel bow shock. *Journal of Geophysical Research*, *110*(A12), 1–13. https://doi.org/10.1029/2005JA011243

Liu, T. Z., Hietala, H., Angelopoulos, V., Omelchenko, Y., Roytershteyn, V., & Vainio, R. (2019). THEMIS observations of particle acceleration by a magnetosheath jet-driven bow wave. *Geophysical Research Letters*, *46*, 7929–7936. https://doi.org/10.1029/2019GL082614

Liu, T. Z., Hietala, H., Angelopoulos, V., Omelchenko, Y., Vainio, R., & Plaschke, F. (2020). Statistical study of magnetosheath jet-driven bow waves. *Journal of Geophysical Research: Space Physics*, *125*, e2019JA027710. https://doi.org/10.1029/2019JA027710

Omelchenko, Y. A. (2015). Formation, spin-up, and stability of field-reversed configurations. *Physical Review E*, *92*, 023105. https://doi.org/10.1103/PhysRevE.92.023105

Omelchenko, Y. A., Chen, L.-J., & Ng, J. (2020). *Dataset for "3D space-time adaptive hybrid simulations of magnetosheath high-speed jets"*. Zenodo. https://doi.org/10.5281/zenodo.4321356

Omelchenko, Y. A., Chen, L.-J., & Ng, J. (2021). *Movies for "3D space-time adaptive hybrid simulations of magnetosheath high-speed jets"*. Zenodo. https://doi.org/10.5281/zenodo.4747515

Omelchenko, Y. A., & Karimabadi, H. (2006a). Event-driven, hybrid particle-in-cell simulation: A new paradigm for multi-scale plasma modeling. *Journal of Computational Physics*, *216*(1), 153–178. https://doi.org/10.1016/j.jcp.2005.11.029

Omelchenko, Y. A., & Karimabadi, H. (2006b). Self-adaptive time integration of flux-conservative equations with sources. *Journal of Computational Physics*, *216*(1), 179–194. https://doi.org/10.1016/j.jcp.2005.12.008

Omelchenko, Y. A., & Karimabadi, H. (2007). A time-accurate explicit multi-scale technique for gas dynamics. *Journal of Computational Physics*, *226*(1), 282–300. https://doi.org/10.1016/j.jcp.2007.04.010

Omelchenko, Y. A., & Karimabadi, H. (2012). HYPERS: A unidimensional asynchronous framework for multiscale hybrid simulations. *Journal of Computational Physics*, *231*(4), 1766–1780. https://doi.org/10.1016/j.jcp.2011.11.004

Omelchenko, Y. A., & Karimabadi, H. (2021). Intelligent agent-based technology for simulation of multiscale systems. In *Space Plasma Simulation Series*. Springer.

Omelchenko, Y. A., Roytershtyen, V., Chen, L.-J., Ng, J., & Hietala, H. (2021). HYPERS simulations of solar wind interactions with the Earth's magnetosphere and the Moon. *Journal of Atmospheric and Solar-Terrestrial Physics*, *215*, 105581. https://doi.org/10.1016/j.jastp.2021.105581

Omidi, N., Berchem, J., Sibeck, D., & Zhang, H. (2016). Impacts of spontaneous hot flow anomalies on the magnetosheath and magnetopause. *Journal of Geophysical Research: Space Physics*, *121*, 3155–3169. https://doi.org/10.1002/2015JA022170

Omidi, N., Blanco-Cano, X., Russell, C., & Karimabadi, H. (2004). Dipolar magnetospheres and their characterization as a function of magnetic moment. *Advances in Space Research*, *33*, 1996–2003. https://doi.org/10.1016/j.asr.2003.08.041

Palmroth, M., Hietala, F., Archer, M., Karlsson, T., Blanco-Cano, X., Turc, L., et al. (2018). Magnetosheath jet properties and evolution as determined by a global hybrid-Vlasov simulation. *Annales Geophysicae*, *36*, 1171–1182. https://doi.org/10.5194/angeo-36-1171-2018

Palmroth, M., Raptis, S., Suni, J., Karlsson, T., Turc, L., Johlander, A., et al. (2021). Magnetosheath jet evolution as a function of lifetime: Global hybrid-Vlasov simulations compared to MMS observations. *Annales Geophysicae*, *39*, 289–308. https://doi.org/10.5194/angeo-2020-49

Plaschke, F., Hietala, H., & Angelopoulos, V. (2013). Anti-sunward high-speed jets in the subsolar magnetosheath. *Annales Geophysicae*, *31*, 1877–1889. https://doi.org/10.5194/angeo-31-1877-2013

Plaschke, F., Hietala, H., & Vörös, Z. (2020). Scale sizes of magnetosheath jets. *Journal of Geophysical Research: Space Physics*, *125*, e2020JA027962. https://doi.org/10.1029/2020JA027962

Plaschke, F., Hietala, M., Blanco-Cano, X., Kajdič, P., Karlsson, T., Sibeck, D., et al. (2018). Jets downstream of collisionless shocks. *Space Science Reviews*, *214*(81), 1–77. https://doi.org/10.1007/s11214-018-0516-3

Raptis, S., Karlsson, T., Plaschke, F., Kullen, A., & Lindqvist, P.-A. (2020). Classifying magnetosheath jets using MMS: Statistical properties. *Journal of Geophysical Research: Space Science*, *125*, e2019JA027754. https://doi.org/10.1029/2019JA027754

Vuorinen, L., Hietala, H., & Plaschke, F. (2019). Jets in the magnetosheath: IMF control of where they occur. *Annales Geophysicae*, *37*, 689–697. https://doi.org/10.5194/angeo-37-689-2019

Winske, D., Yin, L., Omidi, N., Karimabadi, H., & Quest, K. (2003). Hybrid simulation codes: Past, present and future—A tutorial. In J. Büchner, M. Scholer, & C. T. Dum (Eds.), *Space plasma simulation* (Vol. 615, pp. 136–165). Berlin, Heidelberg: Springer Berlin Heidelberg. https://doi.org/10.1007/3-540-36530-3_8